RESEARCH ARTICLE SUMMARY

GAS GIANT PLANETS

Chemical interactions between Saturn's atmosphere and its rings

J. H. Waite Jr.*†, R. S. Perryman†, M. E. Perry†, K. E. Miller†, J. Bell, T. E. Cravens, C. R. Glein, J. Grimes, M. Hedman, J. Cuzzi, T. Brockwell, B. Teolis, L. Moore, D. G. Mitchell, A. Persoon, W. S. Kurth, J.-E. Wahlund, M. Morooka, L. Z. Hadid, S. Chocron, J. Walker, A. Nagy, R. Yelle, S. Ledvina, R. Johnson, W. Tseng, O. J. Tucker, W.-H. Ip

INTRODUCTION: Past remote observations of Saturn by Pioneer 11, Voyager 1 and 2, Earth-based observatories, and the Cassini prime and solstice missions suggested an inflow of water from the rings to the atmosphere. This would modify the chemistry of Saturn's upper atmosphere and ionosphere. In situ observations during the Cassini Grand Finale provided an opportunity to study this chemical interaction.

RATIONALE: The Cassini Grand Finale consisted of 22 orbital revolutions (revs), with the closest approach to Saturn between the inner D ring and the equatorial atmosphere. The Cassini Ion Neutral Mass Spectrometer (INMS) measured the composition of Saturn's upper atmosphere and its chemical interactions with material originating in the rings.

RESULTS: Molecular hydrogen was the most abundant constituent at all altitudes sampled. Analysis of the atmospheric structure of H_2 indicates a scale height with a temperature of 340 ± 20 K below 4000 km, at the altitudes and near-equatorial latitudes sampled by INMS.

Water infall from the rings was observed, along with substantial amounts of methane, ammonia, molecular nitrogen, carbon monoxide, carbon dioxide, and impact fragments of organic nanoparticles. The infalling mass flux was calculated to be between 4800 and 45,000 kg s^{-1} in a latitude band of 8° near the equator.

The interpretation of this spectrum is complicated by the Cassini spacecraft's high velocity of 31 km s^{-1} relative to Saturn's atmosphere. At this speed, molecules and particles have 5 eV per nucleon of energy and could have fragmented upon impact within the INMS antechamber of the closed ion source. As a result, the many organic compounds detected by INMS are very likely fragments of larger nanoparticles.

Evidence from INMS indicates the presence of molecular volatiles and organic fragments in the infalling material. Methane, carbon monoxide, and nitrogen make up the volatile inflow, whereas ammonia, water, carbon dioxide, and organic compound fragments are attributed to fragmentation inside the instrument's antechamber of icy, organic-rich grains. The observations also show evidence for orbit-to-orbit variations in the mixing ratios of infalling material; this suggests that the source region of the material is temporally and/or longitudinally variable, possibly corresponding to localized source regions in the D ring.

CONCLUSION: The large mass of infalling material has implications for ring evolution, likely requiring transfer of material from the C ring to the D ring in a repeatable manner. The infalling material can affect the atmospheric chemistry and the carbon content of Saturn's ionosphere and atmosphere. ■

ON OUR WEBSITE

Read the full article at http://dx.doi.org/10.1126/science.aat2382

The list of author affiliations is available in the full article online.
*Corresponding author. Email: hwaite@swri.edu
†These authors contributed equally to this work.

Cite this article as J. H. Waite Jr. *et al.*, *Science* **362**, eaat2382 (2018). DOI: 10.1126/science.aat2382

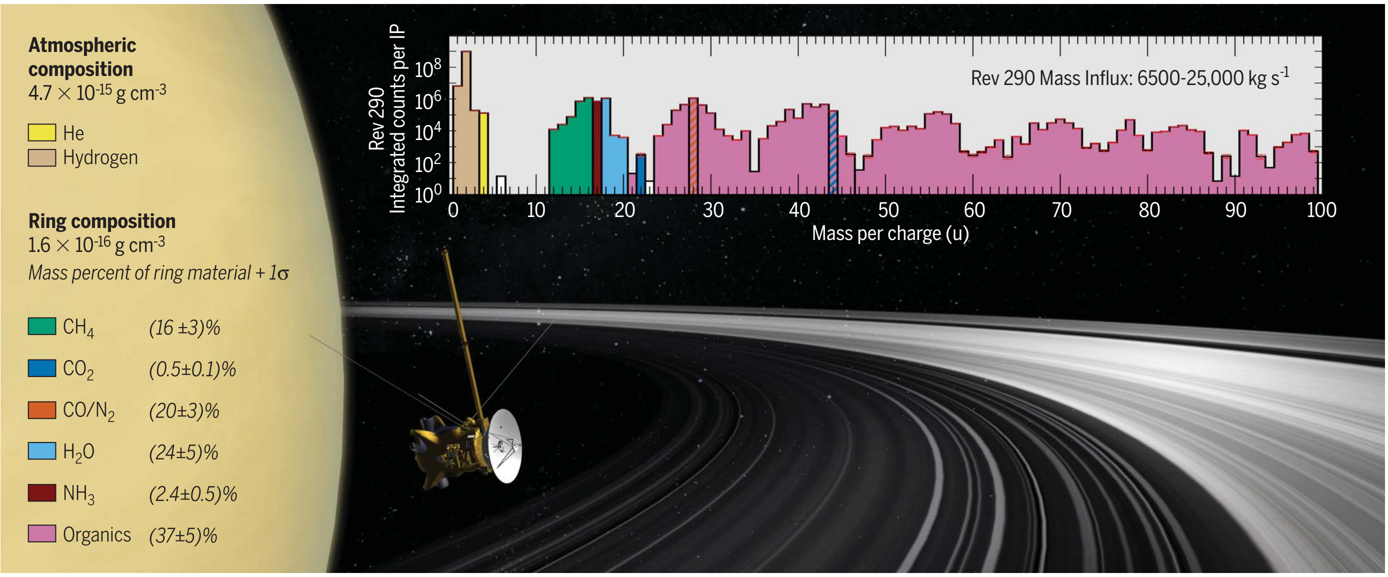

INMS mass spectra from the Grand Finale. The graphic depicts the Cassini spacecraft as it passes from north to south between Saturn and its rings. The inset spectrum shows the mass deconvolution of compounds measured by INMS on rev 290. The *x* axis is in units of mass per charge (u) and extends over the full mass range of INMS (1 to 99 u). The *y* axis is in counts per measurement cycle integrated over the closest-approach data. The mass influx rate for rev 290, derived from mass deconvolution of the rev-integrated spectrum, is shown as embedded text in the spectrum. The side panel gives the average of the mass deconvolution of revs 290, 291, and 292 in mass density units (g cm^{-3}). The composition of the ring-derived compounds in terms of percentage mass density is also shown.

IMAGE COURTESY OF NASA/JPL-CALTECH/SWRI

RESEARCH ARTICLE

GAS GIANT PLANETS

Chemical interactions between Saturn's atmosphere and its rings

J. H. Waite Jr.[1]*†, R. S. Perryman[1]†, M. E. Perry[2]†, K. E. Miller[1]†, J. Bell[3,4], T. E. Cravens[5], C. R. Glein[1], J. Grimes[1], M. Hedman[6], J. Cuzzi[7], T. Brockwell[1], B. Teolis[1], L. Moore[8], D. G. Mitchell[2], A. Persoon[9], W. S. Kurth[9], J.-E. Wahlund[10], M. Morooka[10], L. Z. Hadid[10], S. Chocron[1], J. Walker[1], A. Nagy[11], R. Yelle[12], S. Ledvina[13], R. Johnson[14], W. Tseng[15], O. J. Tucker[4], W.-H. Ip[16]

The Pioneer and Voyager spacecraft made close-up measurements of Saturn's ionosphere and upper atmosphere in the 1970s and 1980s that suggested a chemical interaction between the rings and atmosphere. Exploring this interaction provides information on ring composition and the influence on Saturn's atmosphere from infalling material. The Cassini Ion Neutral Mass Spectrometer sampled in situ the region between the D ring and Saturn during the spacecraft's Grand Finale phase. We used these measurements to characterize the atmospheric structure and material influx from the rings. The atmospheric He/H_2 ratio is 10 to 16%. Volatile compounds from the rings (methane; carbon monoxide and/or molecular nitrogen), as well as larger organic-bearing grains, are flowing inward at a rate of 4800 to 45,000 kilograms per second.

Early modeling of Saturn's atmosphere/ionosphere coupling (*1*) prior to the first radio occultation measurements by Pioneer 11 adopted compositional constraints from Earth-based observations of the well-mixed saturnian atmosphere and used a range of values of the turbulent mixing and heating of the atmosphere based on past planetary observations. Depending on the chosen thermal profile and strength of turbulent mixing, a range of atmospheric and ionospheric conditions were deemed possible (*1*). The "nominal" model of the ionosphere predicted that protons were the primary ion and that the proton's slow radiative recombination reaction was the primary chemical loss pathway, indicating a density of the ionosphere reaching 10^5 cm^{-3}. The modeling suggested that ionospheric composition and structure could serve as a diagnostic of the composition, thermal structure, and turbulent mixing of the upper atmosphere. However, the first radio occultation measurements of the ionosphere made by Pioneer 11 on 1 September 1979 found a peak electron density an order of magnitude lower than predicted for moderate eddy mixing and a warm thermosphere (*2*). The discrepancy was not well understood at the time.

Voyager radio occultation measurements (*3*) supported the low peak ionospheric density and provided independent evidence that the low peak ionospheric density extended into the night side (*4*). It was suggested (*5*, *6*) that water from the rings flowing into the atmosphere could chemically convert protons to molecular H_3O^+ ions at a rate that reproduced the peak electron densities observed by Pioneer and Voyager. The globally averaged water influx rate was estimated to be 4×10^7 cm^{-2} s^{-1}, with localized influx as high as 2×10^9 cm^{-2} s^{-1} (*6*). This proposal of water influx was bolstered by further modeling (*7*, *8*) and ground-based observations of H_3^+ in the Saturn ionosphere (*9*).

The 59 Cassini radio occultations carried out over the course of its prime and solstice missions provided additional data on the ionospheric structure (*8*, *10*). Low latitudes—within 20° of the equator—have lower ionospheric density. Water influx from the rings is a strong candidate to explain the observed latitudinal variations; modeling (*8*) indicates that water influx with a Gaussian distribution about the equator and a peak flux of 5×10^6 cm^{-2} s^{-1} can match the observations obtained prior to the Grand Finale time period.

Observations during the Cassini Grand Finale

The Grand Finale phase of the Cassini mission began on 22 April 2017 with a final close flyby of Titan that diverted the spacecraft to fly 22 times between the planet and its rings. The mission ended on 15 September 2017 after another gravitational deflection by Titan that sent the spacecraft plunging into Saturn's dense atmosphere. Cassini's trajectory between the innermost D ring and the planet allowed in situ coverage of the equatorial ring-atmosphere interaction. Flybys varied in altitude between 1360 and 4000 km above the atmosphere's 1-bar pressure level in three groups (Fig. 1).

The Grand Finale objectives included measuring Saturn's atmospheric H_2 and He and searching for compounds such as water that might indicate an interaction of the upper atmosphere with the main rings. The Ion Neutral Mass Spectrometer (INMS) (*11*) measurements were made several hundred kilometers above the homopause, the level at which turbulent or eddy mixing and molecular diffusion are equal (Fig. 1). In this region, molecular diffusion produces a mass-dependent separation: Lighter compounds have a larger vertical extent due to Saturn's gravity. Prior to the Grand Finale, models and occultation data (*12*, *13*) suggested that H_2, He, and HD were the only neutrals in the upper atmosphere that would be measurable by INMS. The heavier molecule methane was predicted to be present at the ~0.1% level in the well-mixed lower atmosphere (below 1000 km; Fig. 1), but below the detection limits of INMS at the high altitudes sampled by Cassini (*12*, *13*).

Atmospheric composition

INMS obtained measurements of neutral molecules using the Closed Source Neutral (CSN) mode (*11*). INMS operated in a survey mode, acquiring mass spectral data at every mass within its range [1 to 99 atomic mass units (u) at resolution of 1 u], with a repetition rate of 9.5 s (~300 km along track) or 4.5 s (~150 km) when ionospheric data were or were not being acquired sequentially, respectively.

Figure 1 indicates the three altitude regions between the atmosphere and the rings where measurements were made by INMS. Figure 2 shows data for the major atmospheric components H_2, ^4He, and HD + ^3He, separated into those three altitude bands. HD and ^3He have the same atomic mass, so they cannot be measured separately. Because of the geometry of the orbit (rev) for each altitude region, there is a strong correlation between altitude and latitude. The closest approach to Saturn occurred at 4° to 6°S and not at the equator. This allowed us to determine whether the observed compounds are better correlated with a neutral flux from the rings or with Saturn's atmospheric structure (see below). All orbits occurred near local solar noon. This geometry provides complementary

---

[1]Space Science and Engineering Division, Southwest Research Institute, San Antonio, TX 78238, USA. [2]Johns Hopkins University Applied Physics Laboratory, Laurel, MD 20723, USA. [3]National Institute of Aerospace, Hampton, VA 23666, USA. [4]NASA Goddard Space Flight Center, Greenbelt, MD 20771, USA. [5]Department of Physics and Astronomy, University of Kansas, Lawrence, KS 66045, USA. [6]Department of Physics, University of Idaho, Moscow, ID 83844, USA. [7]NASA Ames Research Center, Moffett Field, CA 94035, USA. [8]Center for Space Physics, Boston University, Boston, MA 02215, USA. [9]Department of Physics and Astronomy, University of Iowa, Iowa City, IA 52242, USA. [10]Swedish Institute of Space Physics, SE-751 21 Uppsala, Sweden. [11]Department of Climate and Space Sciences and Engineering, University of Michigan, Ann Arbor, MI 48109, USA. [12]Lunar and Planetary Laboratory, University of Arizona, Tucson, AZ 85721, USA. [13]Space Science Laboratory, University of California, Berkeley, CA 94720, USA. [14]Department of Materials Science and Engineering, University of Virginia, Charlottesville, VA 22904, USA. [15]Department of Earth Sciences, National Taiwan Normal University, Taipei 11677, Taiwan. [16]Institutes of Astronomy and Space Science, National Central University, Chung Li 32054, Taiwan.
***Corresponding author. Email: hwaite@swri.edu** †These authors contributed equally to this work.

information to the Pioneer, Voyager, and Cassini radio occultations, which probed near the dusk and dawn terminators. The Cassini orbits covered a range of Saturn rotational longitudes (Fig. 2). For the low-altitude observations (Fig. 2C), the differences in the shape of the H_2, HD + ^{3}He, and ^{4}He altitude profiles are due to changes in their respective abundances and indicate the effects of diffusive separation via gravity.

H_2 and He data were examined to determine the variability due to altitude, latitude, and orbit, the latter representing temporal and/or longitudinal effects. For each orbit, raw count data were converted to densities (*14*) and an average altitude and density were calculated every 5° latitude using the 11 data points closest in latitude (Fig. 3). Local scale heights were then fitted at each latitude from surrounding data having densities within a factor of $1/(2e)$ higher or lower than the average density, one e-fold about on the latitude of interest.

In addition to local scale heights, a common scale height was calculated using data across all observed altitudes, latitudes, and revs. This was facilitated because altitude and latitude are highly correlated and do not vary much from one orbit to the next. With the exception of 5°N latitude, all altitude/latitude bins are consistent with this common scale height (H), given by $H = kT/(mg)$, where k is Boltzmann's constant, T is the H_2 gas temperature, g is the local acceleration due to gravity, and m is the mass of the gas molecule, H_2 in this case. The common scale height represented in Fig. 3 corresponds to a temperature of 340 ± 20 K. The slopes of the local scale height at 5°N are steeper than the common scale height fit, suggesting a higher temperature. The scale height correspondence between the various altitudes/latitudes sampled, the times/longitudes sampled (on the different revs), and the locally determined scale heights calculated at each point show little evidence for major temporal or spatial atmospheric variation in the region sampled by Cassini during the Grand Finale (*15*).

The analysis of the INMS measurements indicates an atmosphere that has a more complex mass spectrum than predicted by models. There is evidence for both volatile compounds and fragments derived from nanograin impacts in the INMS antechamber. We conclude that the nanograins are sourced from the ring plane. Figure 4 shows the latitude distributions of mass 15 u and mass 28 u in the three distinct altitude ranges. Mass 15 u is the CH_3^+ fragment of methane (mass 16 u is not used because of interference from mass 16 oxygen from water electron impact dissociative ionization), whereas mass 28 u may be derived from N_2, CO, and/or C_2H_4. Mass deconvolution for revs 290, 291, and 292 indicates that less than 10% of the 15 u peak is derived from dissociative fragments from ammonia or heavy organics. From deconvolution of these same spectra, we attribute the fractional contributions of the 28 u signal to be 28% to 58% (average 45%) CO, 41% to 50% (average 46%) N_2, and 0% to 26% (average 9%) C_2H_4, an organic formed from fragmentation of nanograins.

Discrimination between volatile and nanograin-derived signals is achieved by comparing the data in Fig. 4 at the three separate altitude ranges. The uppermost altitude range shows that both mass 28 u and mass 15 u reach a maximum abundance at the equator rather than at the closest-approach latitude (~5°S) with a very large spike for mass 28 u at the equator, which we attribute to the C_2H_4 portion of the peak. The broad latitude extent of the distributions indicates a distributed volatile source in the ring plane. The mass 28 u signal is consistent with C_2H_4 derived from nanograins that have a very narrow Gaussian distribution peaked within 1° of the ring plane at this altitude (~3500 km), comparable to the nanograin distribution seen by the Magnetospheric Imaging Instrument (MIMI) investigation (*16*).

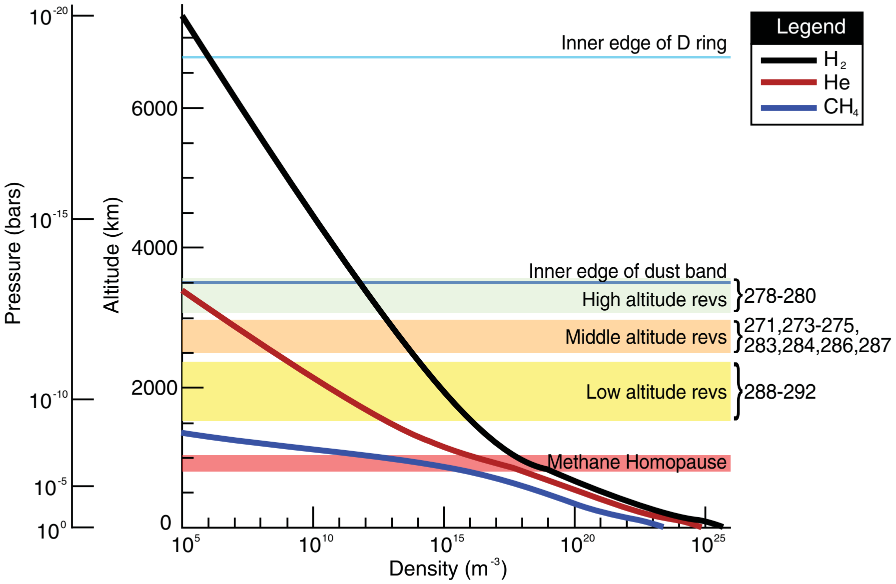

Fig. 1. Predicted structure of Saturn's atmosphere. Density profiles for the major atmospheric constituents H_2, He, and CH_4 (thick curves) were calculated using the hydrostatic model outlined in (*29*). This model was originally developed for Titan but has been modified for Saturn by altering the gravity calculation by including the centrifugal acceleration at the equator, assuming the mean thermal structure determined by Cassini observations (*35*), updating the molecular and eddy diffusion coefficients (*7*), and adjusting the composition at the lower boundary to 13.55% He, 0.45% CH_4, and 86% H_2 (*35*). Overlain are the altitudes at closest approach for the Grand Finale orbits (revs), which form three groups.

Table 1. Mass influx values and composition of inflowing ring material. Density and composition values are the average of revs 290, 291, and 292.

	Mass influx (kg s^{-1})	
Rev number	**Minimum**	**Maximum**
290	6,500	25,000
291	12,000	45,000
292	4,800	18,000

Source	**Density**	**Source composition (mass fraction ± 1σ uncertainty)**
Saturn's atmosphere	4.7×10^{-15} g cm^{-3}	Hydrogen: 99.95 ± 0.01% Helium: 0.05 ± 0.01%
Inflowing ring material	1.6×10^{-16} g cm^{-3}	Methane: 16 ± 3% Ammonia: 2.4 ± 0.5% Water: 24 ± 5% CO/N_2: 20 ± 3% Carbon dioxide: 0.5 ± 0.1% Organics: 37 ± 5%

Both the mass 15 u and mass 28 u compounds also have a component that has begun to spread in latitude toward the closest-approach latitude (4° to 6°S) even at the highest altitudes measured. This is more obvious for mass 15 u than for mass 28 u. This spreading indicates that collisions between the volatile ring components and the saturnian atmosphere (H_2 and He) are beginning to "diffusively couple" the volatiles into the atmosphere as they flow from the rings. At the measured atmospheric densities for this altitude range, diffusive coupling can only occur with molecular volatiles and not heavier nanograins. The latter undergo a smaller relative momentum exchange with the predominantly light hydrogen atmosphere. In the lower-altitude bands, the equatorial peaks disappear as both volatiles and nanograins are diffusively coupled into the atmosphere at the correspondingly higher atmospheric densities. This can be seen for the lower-altitude bands as

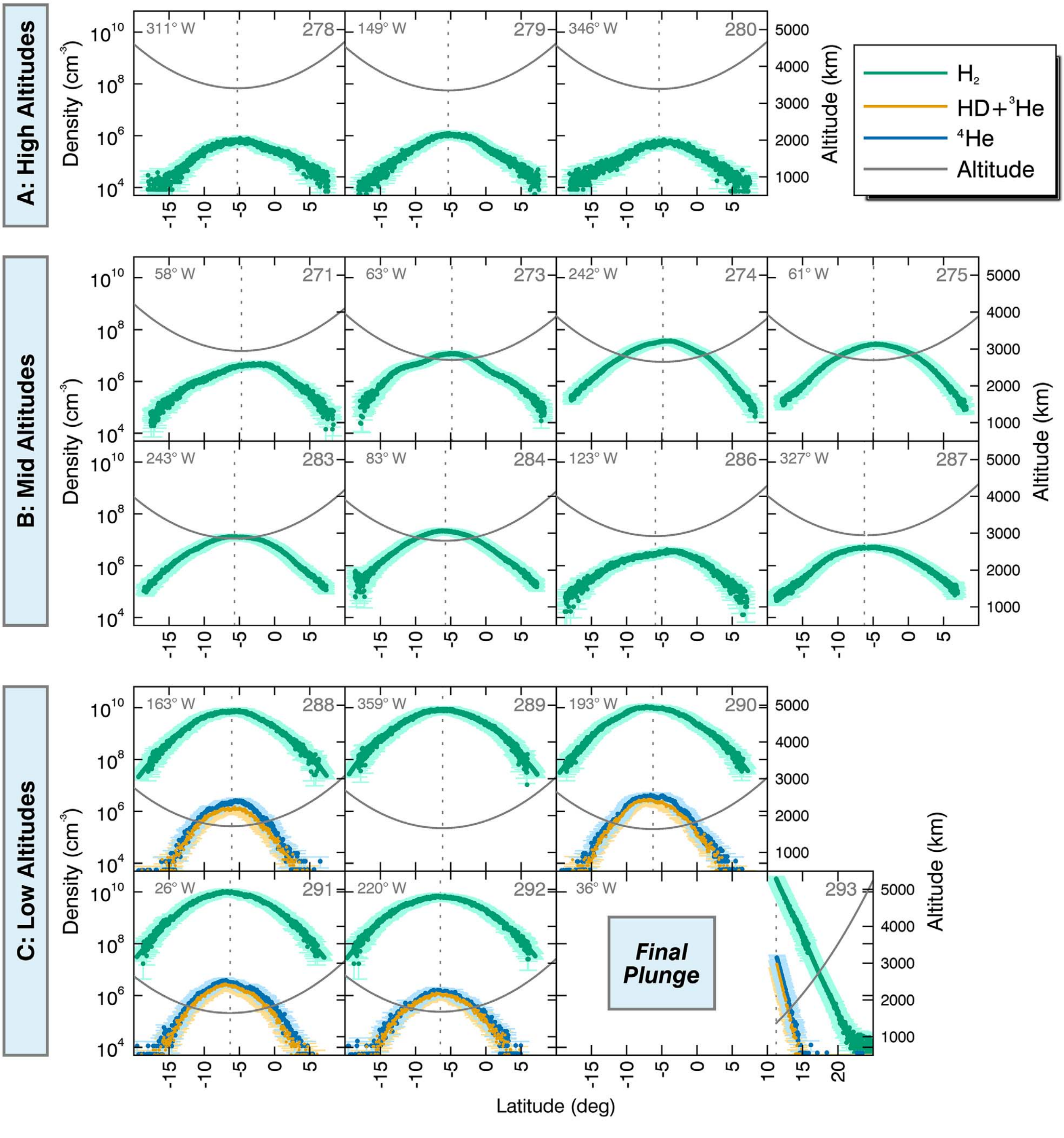

Fig. 2. Major atmospheric gases observed by INMS. The measured densities (points, with shading representing the 1σ uncertainty) of H_2, ^{4}He, and HD + ^{3}He are shown along the spacecraft trajectory for all INMS observations during the Grand Finale. (**A** to **C**) Data are grouped into the three altitude bands denoted in Fig. 1. The signal-to-noise ratios for the highest two altitude bands are too low to allow measurement of He or HD + ^{3}He. The latitude is indicated on the lower axis, and closest approach is denoted by the vertical dotted lines. The spacecraft altitudes above the 1-bar pressure level are shown by the gray curves. The spacecraft moves from right to left in each plot. The corotation longitude and rev number are shown in the upper left and upper right corner of each plot, respectively. The final plunge into the atmosphere is labeled; the telemetry from the spacecraft ended at ~1360 km above the 1-bar pressure level.

the peak distributions of masses 28 u and 15 u shift into alignment with the closest-approach latitude near 5°S. The lowest-altitude band shows symmetric distributions of masses 15 u and 28 u. Their variation with latitude and altitude indicates that masses 15 u and 28 u are dominated by diffusive interaction with the H_2 atmosphere and are free-falling at a terminal velocity, dictated by the increasing hydrogen density and its slowing of the gas. Thus, as the altitude decreases and the background atmosphere increases in density, the maximum diffusion velocity decreases and the infalling material density increases to maintain flux continuity (apart from small effects at this altitude due to chemical loss and latitudinal spreading). This process allows us to estimate the diffusion velocity and determine the material's influx rate from the measured densities (see below).

Figure 4D reinforces the interpretation that the observed compounds originated in the rings. It indicates that for mass 15 u (CH_3 from methane), mass 28 u (CO, N_2, and C_2H_4), mass 44 u (CO_2 and propane), and a surrogate heavier mass from nanograin fragments at 78 u (benzene), the relative abundances are highest at the highest altitudes and reach a near-constant relative abundance below 2500 km as the material is diffusively coupled into Saturn's atmosphere.

Although the solar local time does not vary, the Saturn longitude does change from one orbit to the next. The abundance and distribution of methane, one of the major influx volatiles, varies by a factor of 3 about the average abundance (Fig. 4D, lowest-altitude values). These orbit-to-orbit variations indicate a spatial or temporal change of the volatile source on time scales that are faster than the horizontal diffusion time scale. However, there is no simple variability associated with Saturn's corotational longitude. There is a tentative link to longitudinal variations in the D68 ringlet near the inner edge of the D ring, in which a series of bright clumps appeared in 2015 (*17*) (Fig. 5). An influx that is spatially concentrated near the clumps may in part explain the spatial and/or temporal variations.

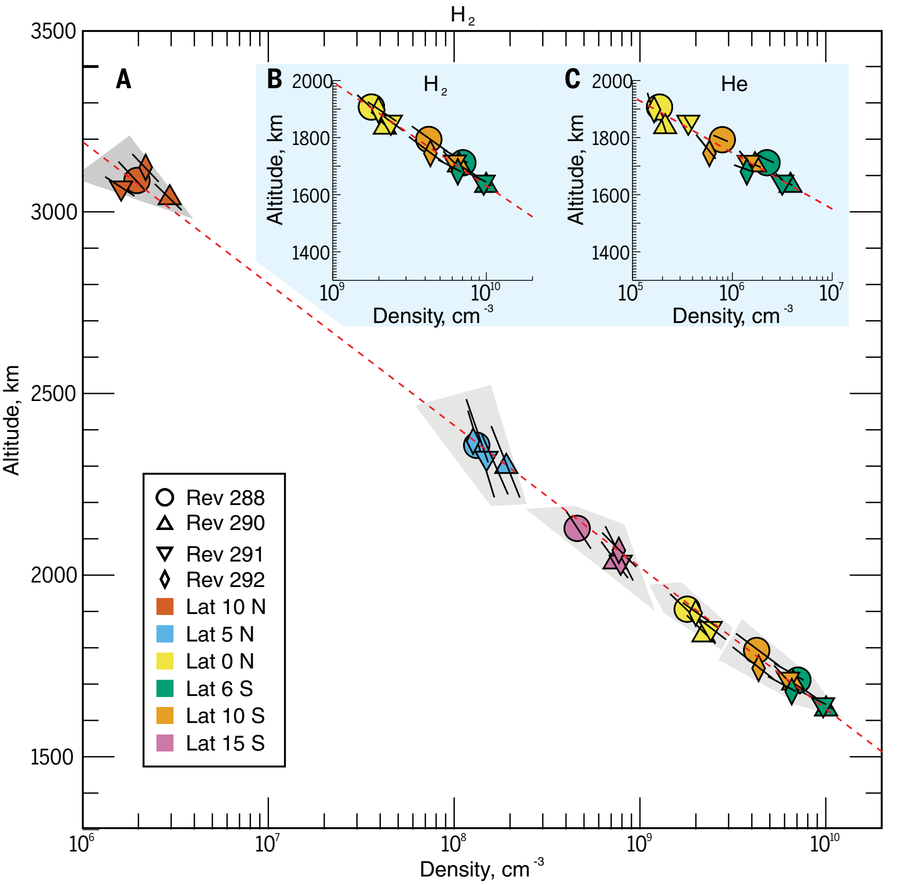

Fig. 3. Variation of H_2 and He with altitude and latitude. (**A**) H_2 densities (points) and locally determined scale heights (lines with 1σ uncertainty shaded in gray) for the altitude/latitude pairs at 10°N (orange), 5°N (light blue), 0° (yellow), closest approach (~5°S, green), and 10°S (brown) for revs 288, 290, 291, and 292 (denoted with different symbols). The common scale height (dashed red line) was determined by a least-squares fit to the density points; it is consistent with all the data except the scale heights at 5°N. (**B** and **C**) Zoomed versions include common scale heights of the lowest altitudes for H_2 (B) and He (C). The common scale heights (dashed red lines) show the 2:1 relation of H_2 to He expected for an isothermal atmosphere in diffusive equilibrium.

Impact fragmentation

The inflowing ring material impacted the INMS antechamber at 29 to 31 km s^{-1} (five times the speeds for which INMS was designed), leading to uncertainty in both absolute abundances and identification of the molecular species. At 31 km s^{-1}, molecules and nanoparticles carry 5 eV of kinetic energy for each atomic mass unit, which in some cases would have been sufficient to dissociate incoming particles and molecules as they impacted the CSN antechamber. However, studies of surface-induced dissociation [e.g., (*18*)] indicate that only about 25% of the impact energy is converted to internal energy of the molecule in the collision process. For H_2 this translates into ~2.5 eV, which is below its dissociation energy of 4.75 eV. Laboratory studies of dissociation in molecule-surface collisions (*19*) suggest that the interaction of H_2 with passive surfaces such as Ag proceeds as a direct interaction with surface atoms. These atomic interactions have a strong angular dependence, with a 10-eV neutral beam having a probability of dissociation of 50% for collinear collisions and >50% for perpendicular collisions. Interaction with a raw Ti surface, such as the CSN antechamber wall after fresh material is exposed through a grain impact, can lead to chemical adsorption (chemisorption) that produces metal hydrides (*20*). Chemisorption processes can also play a role with active metal surfaces or with oxygen-bearing compounds. Therefore, for H_2, CH_4, NH_3, and N_2, the effects of chemisorption in the fragmentation are likely moderate in our case, whereas for H_2O, CO, and CO_2, chemisorption/fragmentation will likely affect our measurements. For example, some of the CO observed at mass 28 u may be an impact fragment from CO_2, which does not affect our main conclusions. Impact fragmentation of CH_4 to produce CH_3 will likely result in reformation of CH_4 on the surface due to the high content and rapid movement of H radicals on the surface in this hydrogen-rich environment. Similarly, CH_3 terminal groups from larger organics may also add to the methane signature, but because heavy organic compounds are at least an order of magnitude less abundant, this can increase the derived CH_4 value by at most 10%. Furthermore, this increase will be compensated by a decrease as a result of CH_4 impact fragmentation that forms CH and CH_2 fragments, which are lost from the antechamber before they can pick up two hydrogens in separate surface reactions because the surface coverage is relatively low (<30%). The net result is that we expect that the CH_4 statistical uncertainty encompasses the additional systematic uncertainties from various fragmentation processes.

The possibility of particle fragmentation inside the closed source does not affect our main conclusions about Saturn's atmospheric structure. With regard to H_2, the agreement of the outbound and inbound data for each orbit examined (290, 291, and 292) below 3000 km and the common scale heights observed at all altitudes, latitudes, and orbits (Fig. 3A) indicate that the effects of dissociation are limited and do not affect the derived atmospheric structure below 3500 km. However, H_2 densities of 10^6 cm^{-3} in an extended outbound region above 4000 km have a constant slope (with density decreasing versus time and altitude) that tracks with the decay of water, which is known to adsorb to the instrument walls (*21*). This correlation suggests that grains have sputtered some raw Ti into the antechamber, allowing hydride formation on the antechamber surface. This hydrogen may have been subsequently displaced by the oxygen from water molecules (TiO and TiO_2 are more tightly bound than the metal hydride) clinging to the antechamber walls after the flyby, thereby creating a low level of H_2 production. This precludes the use of values for H_2 on the outbound phase above 4000 km, but does not affect our other results. However, the loss of water reacting with Ti vapor does suggest that the water abundance may be as

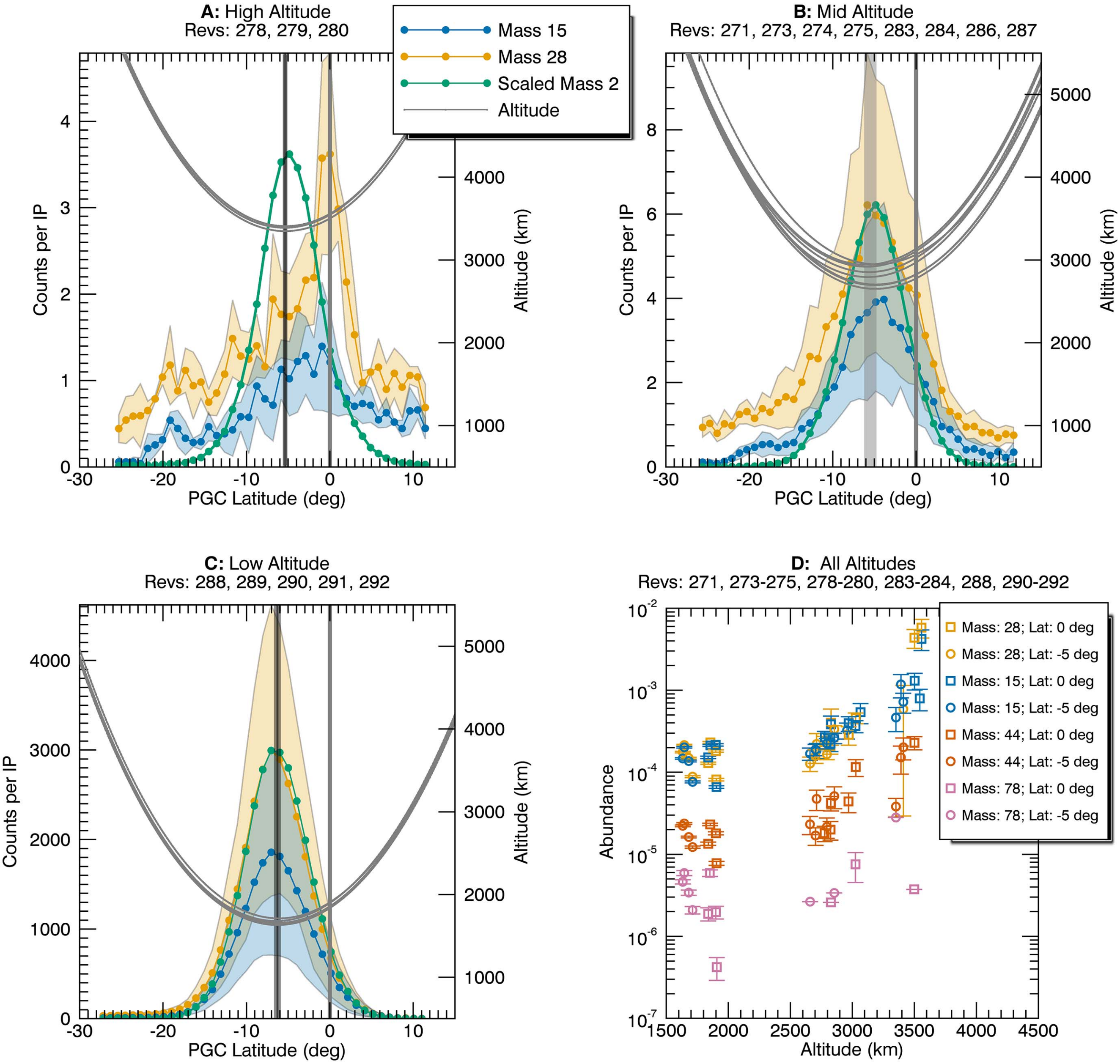

Fig. 4. Volatile inflow from the rings. (**A** to **C**) Plots of latitude and altitude relative to 1 bar for the 15 u and 28 u mass spectral features [in counts per 31-ms integration period (IP) with 1σ uncertainty as colored shading] averaged over each altitude band. The mass 2 u counts (scaled to match the 28 u peak value) are also provided for reference. The high-altitude band comprises revs 278 to 280 (A); the mid-altitude band, revs 271, 273 to 275, 283, 284, 286, and 287 (B); and the lowest-altitude band, revs 288 to 292 (C). The distributions shift in latitude from 0° to closest approach (~5°S) as altitudes decrease. The mass 28 u feature in the highest-altitude bin has both a broad latitude feature, like the 15 u feature, and a sharp spike at the equator indicating contributions from both volatiles (CO and/or N_2) and grains (C_2H_4 fragments from organic grain impacts). (**D**) Abundances (with 1σ error bars) for 28 u (carbon monoxide, molecular nitrogen, and ethylene), 15 u (methane), 44 u (carbon dioxide plus a propane impact fragment), and 78 u (a benzene impact fragment) as a function of altitude at the equator (squares) and at 5°S latitude (circles). The equatorial latitude is the location of ring plane influx, whereas 5°S latitude represents the closest approach to the atmosphere as a result of the flyby geometry (see Fig. 2).

much as 30% larger than reported in Table 1 and Fig. 6. Because the deuterium hydride has a lower activation barrier for formation than the H hydride ([*20*]), which led to H/D fractionation during the flyby, the present dataset is difficult to use for studying the H/D ratio of the atmosphere and rings.

The strongest evidence that CH_4 and N_2 are not simply by-products of fragmentation of heavy compounds, but instead native volatile gases, comes from the latitude distributions of mass 15 u and mass 28 u at the highest altitudes (3500 to 4000 km; see Fig. 4 and related text). The mass 15 u (methane) and mass 28 u signals both show a broad latitude distribution running from 20°S to 10°N latitude but differ in peak location; this finding constitutes evidence for a latitudinal spread of the native volatile compounds (CO and N_2), combined with C_2H_4 impact fragments of the organics nanograins from the peak near the ring plane. This leads us to conclude that methane, nitrogen, and carbon monoxide are native volatiles originating in the rings. However, we cannot rule out the possibility that some of the carbon monoxide is a fragment by-product of carbon dioxide, for which we also have evidence in the spectra. We have no corresponding evidence for the presence of water, carbon dioxide, or ammonia. They may be native volatiles or fragments from nanograins. Given our uncertainty of the fragmentation processes, it is fortunate that this rough classification between native volatiles and fragments derived from nanograins has no effect on the mass inflow flux we derive below, although it does affect how these compounds react chemically with the atmosphere and ionosphere.

A plethora of organics

INMS spectra from Saturn's exosphere include signal over the full range of neutral masses, up to 99 u (Fig. 6). Species with mass exceeding 46 u are present in all six of the final low-altitude orbits, consistent with a local source for this material. The count rate distributions are highest around 16 u, 28 u, 44 u, 56 u, and 78 u, indicating an organic-rich spectrum. These spectra are more complex than predicted by models, with contributions from many different chemical compounds.

Our assessment of the composition of the inflowing material observed on revs 290, 291, and 292 gives the following fractions by weight: methane, 16 ± 3%; ammonia, 2.4 ± 0.5%; water, 24 ± 5%; molecular nitrogen and carbon monoxide (CO/N_2), 20 ± 3%; carbon dioxide, 0.5 ± 0.1%; and organic compounds, 37 ± 5%. The values reported are the mean of the orbits analyzed. To account for physical adsorption (physisorption) and chemisorption to the instrument walls ([*21*]), we generated integrated spectra (Fig. 6). For masses with a high tendency to interact with the walls of the antechamber (those in rev 290 with a ratio of outbound to inbound counts greater than 2 at 1750 km and with a maximum count rate greater than 40), the integrated spectra show the integrated signal at each mass over the full time period for which the signal at 18 u is above the background level. The remaining masses are integrated using the time window from 500 s before to 500 s after closest approach. We used a standard fitting procedure ([*22*]). Using data from calibrations of the INMS engineering model and the National Institute of Standards and Technology mass spectral library ([*23*]) to determine the dissociative fragmentation patterns and absolute calibration, we constrain the abundances of carbon dioxide, CO/N_2, water, ammonia, methane, hydrogen, and helium for each integrated spectrum. The remaining counts at masses ≥12 u are attributed to organic species. Some signal may be due in part to inorganic S-bearing species such as H_2S or SO_2; however, the overall abundance of these compounds is consistently < 0.1% by mass of the inflowing material and less than our quoted uncertainties.

The ring particle composition (i.e., compounds other than H_2 and He) is approximately 37 weight percent (wt %) organic compounds heavier than CH_4. The other abundant ring particle compounds are water, CO/N_2, methane, ammonia, and carbon dioxide. Signals at 12 u and 14 u constrain the abundances of CO and N_2, respectively, and suggest that an inorganic component is likely present at 28 u. However, the value for CO reported is an upper limit, as the constraint from 12 u does not account for ionization fragments from organics or from impact fragmentation of CO_2 internal to the instrument. The organic fraction itself is fitted well by hydrocarbons, but the

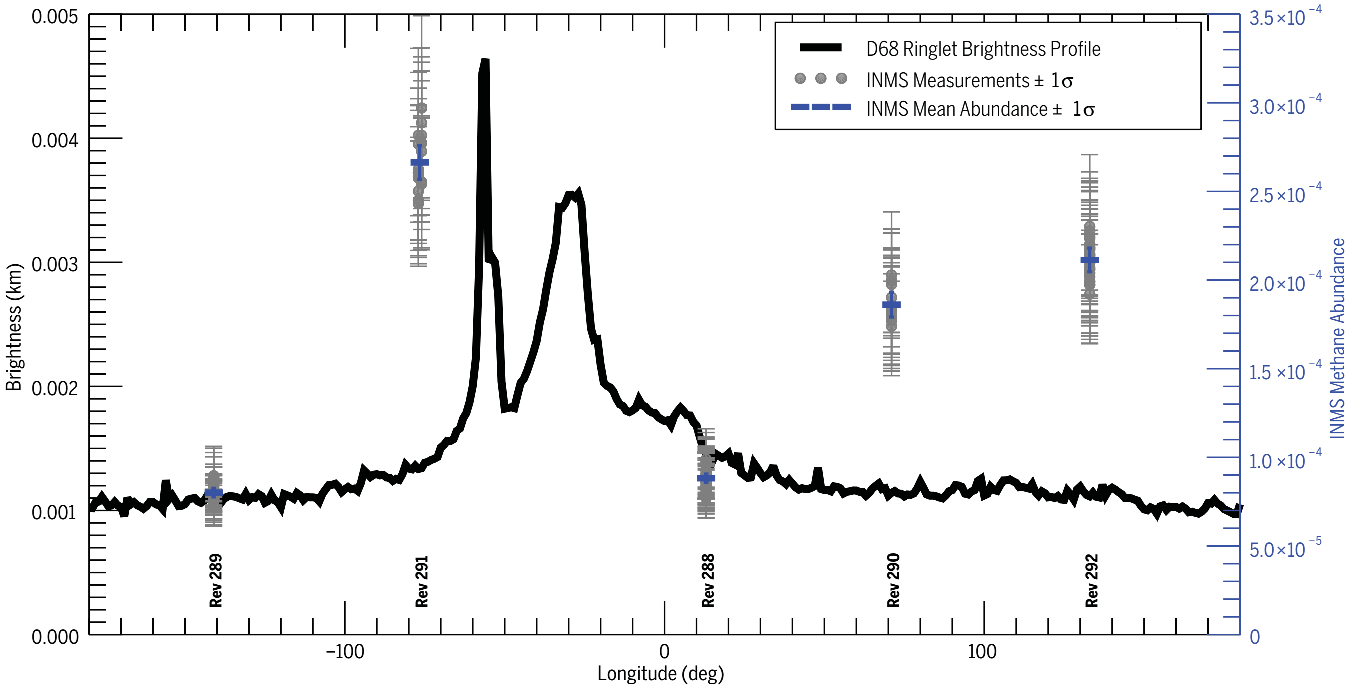

Fig. 5. Relationship between lower-altitude methane abundances and the reflected brightness of the D68 ringlet. The radially integrated brightness of the D68 ringlet (black line; see methods section) is plotted as a function of the Keplerian longitude associated with the clumps in the D68 ringlet, which has a radial distance of 67,630 km and an orbital period of 4.93 hours. Reported brightness is relative; the measurement is unitless but once integrated radially is provided in km. Overlain are the abundances (right axis) for methane observed by INMS between 1725 and 1750 km altitude on inbound in the low-altitude revs (288 to 292; gray points) and their mean at each longitude (blue rectangle with 1σ uncertainty). The highest abundances occur for rev 291, just behind the brightest parts of D68.

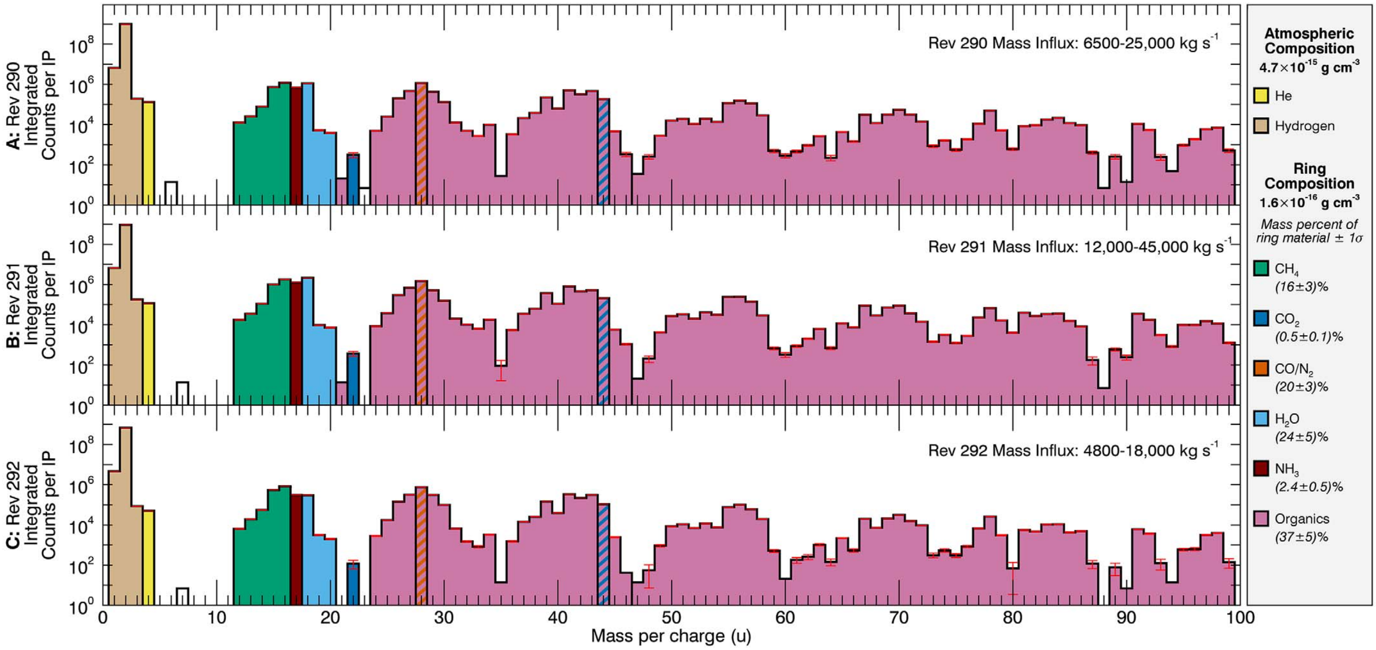

Fig. 6. Integrated mass spectra for the last three orbits of the Grand Finale. (**A** to **C**) Background-subtracted data integrated over the flyby are shown for revs 290, 291, and 292 along with 1σ error bars (red, in most cases narrower than plotting line). INMS has unitary mass resolution. The *y* axis is in counts per integration period (IP, 31 ms) integrated over the closest-approach data. The coloring corresponds to the dominant parent molecule for each mass. Masses 28 u and 44 u are both dominated by multiple components: CO/N_2 plus organics (28 u) and CO_2 plus organics (44 u). The side panel gives deconvolved mass density: H_2 and He from the atmosphere; and other compounds from the rings, whose percentage contributions to the ring material are also shown. The mass influx rate for each rev is shown at the top right of each panel. Mass influx rates and composition are summarized in Table 1.

presence of O- or N-bearing organics is not excluded. Water, 28 u, and methane are the most abundant volatiles with ratios relative to H_2 on the order of 10^{-4} for the integrated spectra. The spectra are also consistent with the presence of aromatic species, including the possible signal of benzene at 78 u. We estimate that the total organic mass density is on the order of 10^{-16} g cm^{-3}. The organic compounds identified may be either indigenous compounds present in the atmosphere or the products of high-speed impacts with INMS (see above). In either case, these spectra suggest abundant native organic material. The mass of hydrocarbons detected by INMS is equivalent to the mass of ~10^6 cm^{-3} nanoparticles with masses in the range detected by MIMI (*16*). Because MIMI detected far fewer particles, most of the mass measured by INMS appears to be below the 8000 u lower measurement limit of MIMI (*24*).

Masses above ~70 u are poorly fit by compounds with primary masses in the range of INMS. Because studies of heavy extraterrestrial organics indicate that these heavier organic compounds include aromatics [e.g., (*25*)], common aromatic molecules such as naphthalene were added to the spectral library as candidate parent species for this region. Compounds produced by ice irradiation experiments (*26*, *27*) were also considered. We find that this mass region is consistent with the presence of aromatic compounds comprising ~5 to 10 wt % of organics. Aromatic material would be subject to impact dissociation that may yield aliphatic compounds, so this abundance of aromatic material is a lower limit.

Estimating the mass influx in the equatorial region

We estimated the mass influx of material in the equatorial region by combining calculations of the material velocities and densities. From the mass deconvolution described above, we estimated the densities of methane, water, ammonia, nitrogen, carbon monoxide, carbon dioxide, and organic fragments measured at an altitude of 2000 km during revs 290, 291, and 292 (see Fig. 6). We used two different approaches to determine the appropriate downward diffusion velocity. One is based on the limiting flux equation (*28*):

$$v = \frac{D_{12}}{H}\left(1 - \frac{m_1}{m}\right) \qquad (1)$$

where H is the scale height (we use a value of 150 km based on the INMS data), m_1 is the mass of the minor species of interest, and m is the mean mass of the atmosphere (we use a value of 2 u). D_{12} is the coefficient for diffusion of species 1 in species 2. The alternative approach uses the diffusion coefficients calculated using a simple hydrostatic model adapted from previous work (*29*). The methane diffusion velocity at 2000 km is calculated using both methods for a range of influx values of methane. The maximum (1×10^4 cm s^{-1}) and minimum (4.5×10^3 cm s^{-1}) diffusion velocities are then taken as bounding cases. The diffusion velocities for the other materials are scaled by the ratio to methane of their diffusion coefficients flowing through H_2 (*30*). The range of diffusion velocities used in this calculation is inclusive enough that assumptions about whether methane, ammonia, water, nitrogen, carbon monoxide, and carbon dioxide are present at 2000 km as volatiles or are derived as fragments of a larger organic moiety will have little effect on the diffusion velocity calculation. The equatorial latitude band used in the mass influx calculation is 8° wide, which is the half width of the low-altitude measurements in Fig. 4C. The difference between the maximum and minimum values is completely dominated by the uncertainty of determining the diffusion velocities, which is a systematic uncertainty that is constant from one orbit to the next. The uncertainty due to the densities of the components is ~1%, indicating that there is variation in the mass influx between rev 291 and the other two revs (290 and 292) we analyzed. However, the mass fraction of a given component is not statistically different from orbit to orbit. Calculated mass influx rates for revs 290, 291, and 292 and the average composition of material from Saturn's atmosphere and from ring influx are reported in Table 1 and Fig. 6.

Ionospheric measurements

The open source on the Cassini INMS was designed with the primary purpose of measuring reactive neutrals and ambient ions in Titan's ionosphere and upper atmosphere (*11*), where flyby velocities were in the range of 6 km s^{-1}. However, the Cassini Grand Finale orbits resulted in spacecraft speeds relative to the atmosphere of ~31 km s^{-1}. At these speeds, INMS ion measurements were limited to <8 u. Despite the limited mass range, INMS measurements of light ions can be combined with Radio Plasma Wave Spectrometer (RPWS) measurements of the free electron content (*31*, *32*) to produce a more complete picture of the ionosphere. The INMS open source has a narrow field of view (< 2° cone) relative to the closed source (180° cone). Therefore, the spacecraft must be used to point the instrument into the ram direction to allow measurements of ions. This orientation occurred on a limited set of Grand Finale revs (283, 287, 288, and 292).

Figure 7 shows the ionospheric data obtained by INMS during the Cassini Grand Finale. Figure 7, A and B, shows the mid-altitude band (revs 283 and 287; refer to Fig. 1 for context). These time series indicate that for the altitudes and latitudes covered by these orbits, the free electron density is within a factor of 2 of the INMS measured light ion density. The asymmetry between north and south latitudes above 15° can be attributed to ring shadow effects during the autumnal solstice illumination (*33*). This reduces incoming solar ultraviolet flux, lowering the photoionization, although the effect is somewhat mitigated by the long lifetimes of the H^+ and H_3^+ ions and the associated transport effects. Figure 7, C and D, shows revs 288 and 292 from the lowest set of altitudes, where the near-equatorial ionosphere shows a large difference between the free electron density and the light ion density, indicating the presence of heavier ions (>8 u) that must account for the bulk of the ionospheric density (more than 75% of the ions are >8 u). This heavy-ion region is asymmetric with respect to the equator, ranging in latitude from ~2°N to 12°S. However, it does roughly correlate with the inflow of volatiles and organic nanograins from the D ring discussed above, and closely matches MIMI Charge Energy Mass Spectrometer (CHEMS) measurements of nanoparticles (*16*). The molecular volatiles (water, methane, ammonia, carbon dioxide) can easily convert the long-lived protons of the ionosphere into molecular ions with shorter lifetimes, decreasing the overall electron density (*6*), as described below.

Figure 7E shows additional measurements of the ionosphere for rev 288. The individual light ion concentrations for H^+, H_2^+, H_3^+, and He^+ are indicated. The H^+ and H_3^+ densities decrease in the near-equatorial heavy-ion region, consistent with an inflow of heavier molecules. The H_2^+ ions measured are the primary product of ionization in the Saturn ionosphere and are created by ionization of H_2, the most abundant neutral, by solar extreme ultraviolet radiation (*34*). They are a good tracer of the ionization process. Figure 7E also shows the scaled value of the positive nanoparticles measured by CHEMS (*16*) added to the INMS light ion density. The second-order latitudinal structure of the CHEMS measurements of positive nanoparticles is closely correlated with the free electron density of the bulk ionosphere. Although the scaling factor is ~10^6 and these very large positive ions cannot themselves account for the secondary structure, they represent the positive member of a dusty plasma that contains both neutral nanoparticles and negative-ion nanoparticles, which appears to affect the recombination of the primary positive molecular ions that dominate the equatorial ionosphere.

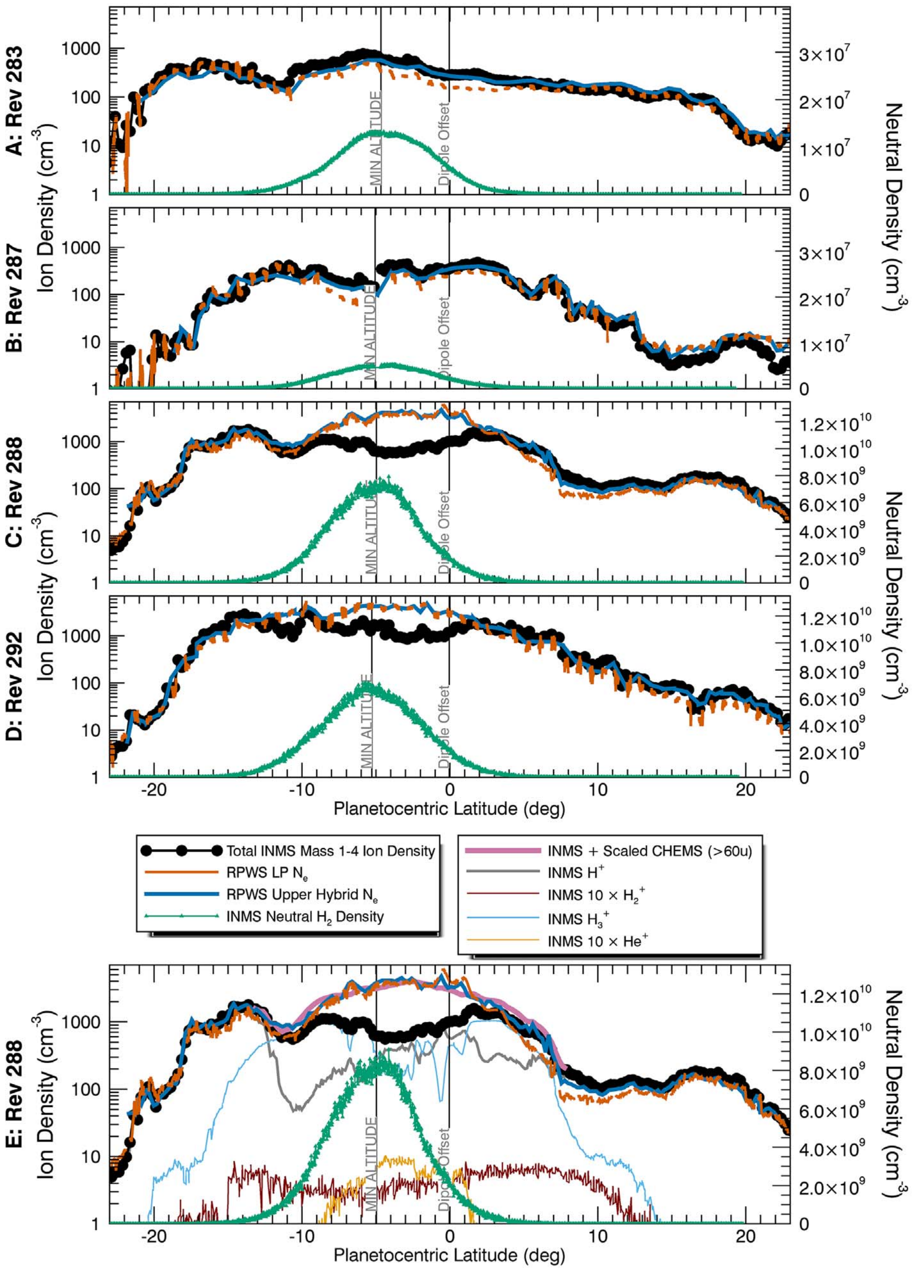

Fig. 7. INMS ionospheric observations during the Grand Finale. (**A** to **D**) Summary data for all four proximal orbits in which INMS obtained ionospheric data. The sum of the light ion densities for masses 1 to 4 u is shown by a black line. The RPWS electron density using the Langmuir Probe (LP) (*31*) is shown in dark orange and using a hybrid method (*32*) with the thick blue line (both on the left axis). The atmospheric H_2 density is shown by a green line (right axis). (**E**) The same data as (C) with the addition of the INMS-measured H^+, H_3^+, H_2^+, and He^+ ion densities (left axis) and the atmospheric H_2 density (right axis). The INMS ion density values are uncertain by about 21% at the ionospheric peak, rising to 25% at ±20° latitude; this is due to the combination of systematic uncertainty in the detector gain (*14*) and the statistical uncertainty. Also shown is the MIMI CHEMS measured nanoparticle positive ion density (*16*) multiplied by 10^6 (pink line) and added to the INMS light ion density, which corresponds to the electron density structure.

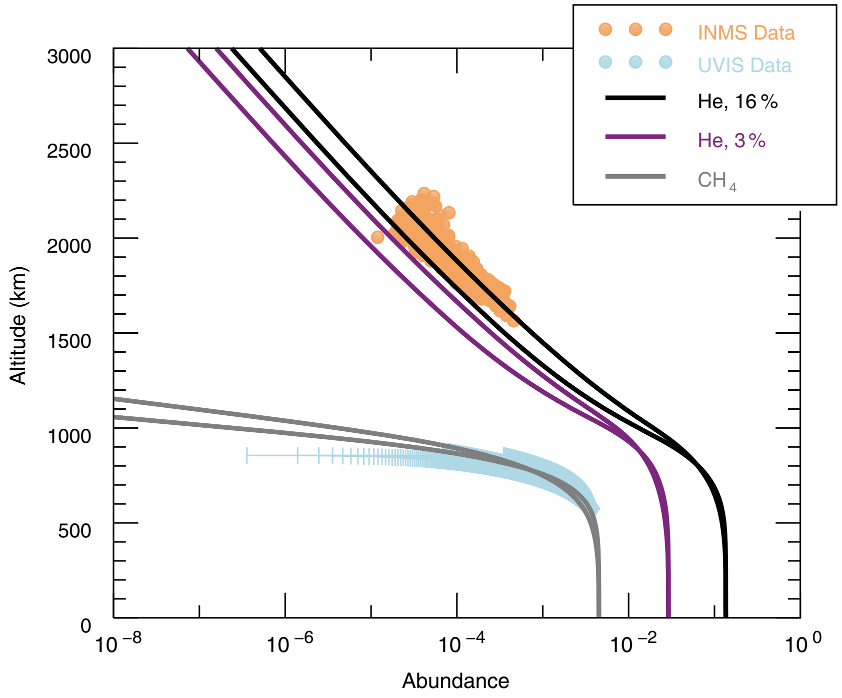

Fig. 8. Relationship of the INMS-measured He/H_2 ratio to the homosphere helium abundance. Altitude-dependent profiles for the abundances of methane (gray curves and light blue dots) and helium (black and purple lines and sandy brown dots) are shown. Methane data are from UVIS; He data are from INMS. Two scenarios for the homosphere He/H_2 ratio are shown: 0.03 in purple (38) and 0.16 in black (35), which is close to the jovian value (4). The solid and dash-dotted lines for each assumed abundance use two different formulations for the turbulent diffusion (eddy diffusion) coefficient (29, 35).

Implications for Saturn's atmosphere and ionosphere

Atmospheric structure

The analyses shown in Figs. 2 and 3 indicate a background atmospheric structure that is consistent with predictions shown in Fig. 1 for both hydrogen and helium. However, species heavier than helium are far more abundant than predicted. The differences between the predicted and observed atmosphere are largely confined to the excess volatiles that we have concluded flow in from the D ring, as discussed below.

The measured hydrogen and helium abundances are compared to the models (35) in Fig. 8. The vertical profiles of the helium and methane abundances calculated by the hydrostatic model (29), which was used to benchmark the nonhydrostatic Global Ionosphere-Thermosphere Model (36, 37), are shown. Methane abundances for altitudes below those observed by INMS are taken from the combination of Cassini Ultraviolet Imaging Spectrograph (UVIS) and Composite Infrared Spectrometer (CIRS) data (35). As can be seen in Fig. 8, the relatively large uncertainties in the methane abundance allow both approaches to reproduce the UVIS/CIRS methane data equivalently well, even though they use widely different versions of the eddy diffusion coefficient.

Also shown in Fig. 8 are two different scenarios for the deep-atmosphere He/H_2 ratio. The purple curves adopt a He/H_2 ratio of 0.03, consistent with a helium abundance of ~0.0291 reported from the Voyager measurements (38). We use the ratio of 0.03 to represent the most likely lower bound for the well-mixed atmosphere value for helium (35). The other set of helium curves represent a He/H_2 ratio in the well-mixed lower-altitude region of the atmosphere of ~0.16 (an abundance of helium of ~0.1355); this value is more consistent with the recent analysis (35), which reports a homosphere abundance of ~0.11 ± 0.02 inferred from UVIS and CIRS data. The latter approach brackets the helium abundances obtained directly from the INMS measurements, whereas the Voyager-derived curves systematically fall below the data (Fig. 8). This comparison suggests that the INMS helium data are more consistent with a nearly jovian homosphere abundance of ~0.1355 (39). In contrast, the model that uses a lower He/H_2 ratio systematically fails to reproduce the INMS data (15).

These results for the homospheric ratio of He/H_2 have implications for understanding the internal structure and evolution of Saturn. The conventional explanation for the excess infrared luminosity of Saturn relative to the expected thermal emission is that cooling over time leads to the demixing of helium from hydrogen, with the heavier helium raining out into the deeper interior and generating heat (40). Our measurements and modeling permit a modest depletion of helium but are inconsistent with a strong depletion relative to the protosolar He/H_2 ratio of 0.19 (41). As an example, the nominal INMS value for the He/H_2 ratio is 0.16 (Fig. 8), which is similar to the value at Jupiter (0.157 ± 0.003) (42). However, some additional helium rain in Saturn beyond that in Jupiter is allowed, as the INMS data are consistent with a He/H_2 ratio as low as 0.10. A range between 0.10 and 0.16 would maintain the viability of helium rain—a process that is consistent with He/H_2 < 0.12 in the well-mixed atmosphere (43)—as the cause of excess luminosity. This range is also consistent with the most recently derived He/H_2 ratio of 0.11 to 0.16 from Voyager (44) and with the Cassini UVIS-CIRS value of 0.09 to 0.13 (35). Overall, the homospheric helium abundance from INMS may be slightly higher than previous estimates, but the uncertainties are large.

Ionospheric structure

The presence of the light-ion species observed by INMS in the ionosphere (H^+, H_2^+, H_3^+, He^+) was predicted almost 40 years ago by a model of a neutral atmosphere dominated by H_2 and He (1). Ion and neutral measurements made by INMS in the ionosphere are consistent in that they both indicate the presence of an additional heavy molecular species (both neutral and ionized) in the equatorial upper atmosphere. Water-group neutral and ion species were predicted, but the present Cassini data indicate that the chemical composition of the material falling inward from the rings is concentrated at the equator, is chemically much more complex than predicted, and includes a substantial organic component, perhaps in the form of nanoparticles.

Dissociative and nondissociative photoionization of molecular hydrogen (and to a lesser degree He) by solar extreme ultraviolet radiation is the source of ionization in the equatorial ionosphere. The H_2^+ and H^+ ions thus produced undergo a series of ion-neutral reactions, generating other ion species such as H_3^+ via the fast reaction $H_2^+ + H_2 \rightarrow H_3^+ + H$. The H_2^+ production rate along the spacecraft track can be determined empirically by multiplying the measured H_2^+ density by the measured H_2 density (both shown for rev 288 in Fig. 7E) and by the rate coefficient of $2 \times 10^{-9}\ \mathrm{cm^3\ s^{-1}}$ (34). The production rate is $\sim 8\ \mathrm{cm^{-3}\ s^{-1}}$ near closest approach. At these altitudes, the effects of approximately 50% opacity in the extreme ultraviolet are evident in the production rate, indicating that the spacecraft's closest approach nearly reached the altitude of peak ion production. This effect is also evident as the dip near closest approach in the H_2^+ densities in Fig. 7.

Figure 7E also shows a broad gap near closest approach between the total light-ion densities measured by INMS and the electron densities measured by RPWS. Assuming quasi-neutrality (that is, the ion density approximately equals the electron density) and neglecting negative ions, this suggests the existence of an ion with a mass beyond the upper limit of the open source for these orbits (8 u). This ion, or collection of ions, is more abundant than light ions in the main ionospheric layer. To maintain consistency with the neutral composition provided by the closed source, the heavy ion cannot be solely a water-derived molecular ion. Simple ion chemistry for the light ions can put limits on the abundance of the heavy neutral ring ions with a large dissociative recombination rate coefficient. The low H^+ and H_3^+ densities measured near closest approach require fast reactions with a molecular volatile at an abundance of approximately 10^{-4} (*34*), consistent with the INMS neutral data. This simple ion analysis does not indicate the identity of the molecular volatile, which likely includes methane, ammonia, water, and carbon dioxide as measured by INMS. These compositional changes are discussed in (*45*).

Simple photochemistry for a single major ion (i.e., H_2^+) states that the total ion production rate equals the ion-electron loss rate from dissociative recombination. This leads to an expression for the electron density N_e:

$$N_e = \left(\frac{P_{H_2^+}}{\alpha}\right)^{1/2} \tag{2}$$

where $P_{H_2^+}$ is the H_2^+ production rate and $\alpha \approx 5 \times 10^{-7}\ cm^3\ s^{-1}$ is a typical dissociative recombination rate coefficient (*46*). Using the peak production rate near closest approach from Fig. 7 yields a photochemical equilibrium value of $N_e \approx 10^4\ cm^{-3}$, in good agreement with the peak electron density measured by RPWS (*31*, *32*). This agreement suggests that the role of negative ions and/or particles in determining the charge balance may be relatively minor.

It is well known in planetary and terrestrial aeronomy (*47*) that chemistry dominates at lower altitudes in an ionosphere, whereas transport processes become important at higher altitudes where the collision frequency is low. We expect this to be true for Saturn's ionosphere as well. The chemical lifetime of the major molecular compounds varies from ~200 s near closest approach up to ~2000 s (i.e., about 30 min) near the upper edge of the heavy-ion gap/layer. The H^+ chemical lifetime should be controlled by the abundance of the heavy neutral compounds, which increases rapidly with altitude, via ion-neutral reactions. Plasma transport is largely constrained to proceed along the magnetic field (*47*), which in the equatorial region is almost horizontal. The H_2^+ production rate sharply falls off by a factor of ~10 in the shadow of the planet's B ring (Fig. 7E), and the H_3^+ density also falls off rapidly. However, the H^+ density, which is equivalent to N_e in this region, falls more slowly. This suggests that H^+ is not in chemical equilibrium in the altitude region near 2000 km and above, but that H^+ plasma is produced outside this region and flows into the shadowed area.

He^+ ions (4 u) are created by the photoionization of atmospheric He, which falls with altitude more rapidly than H_2 because of diffusive separation. Figure 7E shows that the He^+ density decreases more rapidly with altitude than does the H_2^+ density. However, some of the 4 u signal is contributed by H_2D^+.

Origin of volatiles in the thermosphere

Molecular hydrogen and helium, which are sourced from the well-mixed atmosphere via diffusive transport, are the most abundant neutral species in the upper atmosphere of Saturn. The next most abundant category of neutrals by mass is organics, followed by water, mass 28 u inorganics (CO and N_2), and methane (Fig. 6). Methane is too heavy to diffuse upward from the homosphere, so the source of methane must be external (see above). The source of CH_4 seems to be Saturn's rings. One possibility is that an icy carrier of CH_4 (e.g., clathrate hydrate) may be present inside the ring particles, which volatilizes when heated by sunlight or ablation in Saturn's thermosphere. Any CH_4 gas released would diffuse into Saturn's atmosphere under gravity.

The volatile composition observed by INMS appears to be similar to material found in comets (*48*). This could be explained if Saturn's rings were formed from unprocessed primordial ices, derived from a thermally primitive precursor body such as a small icy moon. Alternatively, the similarity may be coincidental if species such as CH_4, NH_3, and CO are major products of the thermal/ultraviolet degradation of complex organics in an H_2-rich environment.

The mass of Saturn's C ring is ~10^{18} kg (*49*), about 0.03 times the mass of Saturn's moon Mimas. Therefore, if we use the mass influx inferred from the INMS measurements (4800 to 45,000 kg s^{-1}), we calculate a lifetime of 700,000 to 7 million years for the C ring. Yet this only reflects today's influx. The current influx is directly from the D ring rather than the C ring, which must be the ultimate supplier because the mass of the D ring [likely no more than 1% of the C ring mass (*50*)] can maintain current loss rates for only 7000 to 66,000 years—a very short amount of time in terms of solar history. It is unclear whether the C ring can lose 1% of its mass into the D ring by viscous spreading over that time period (*51*).

Although viscous spreading of the C ring is likely not the cause of mass transfer to the D ring (*51*), occasional transfer of ~1% of the mass of the C ring into the D ring region via a large ring-tilting event is feasible. These ring-tilting events involve a stream of planet-orbiting rubble crossing the ring plane somewhere in the C or D rings. The C ring provides the ultimate source, containing enough mass to last (at current influx rates) about 5% of the time that the rings themselves have existed (~200 million years) (*52*–*54*). The D ring could be repopulated sporadically by large impact events such as those that tilted the D and C ring plane (*55*). Once enough small particles are brought into the D ring region, exospheric drag would quickly drain them into the planet, as observed by Cassini.

We conjecture that one or more transient events occurred in the recent past that disturbed the D ring, or changed its mass and particle size distributions so that tenuous gas drag can more quickly cause it to fall into the planet. The latest such event appears to have been the one that perturbed the D68 ringlet (*17*). However, the weak correlation shown in Fig. 5 is not compelling. Evidence of ionospheric depletion observed well before the formation of bright clumps in the D68 ringlet suggests that the material inflow may have been taking place for a longer period of time (*2*). Therefore, we examined the evidence for D ring perturbations over a longer time scale.

The D ring structure of irregularly spaced bands or belts has changed markedly since the Voyager flyby (*56*). A pattern within the ring has been interpreted as a vertical spiral ripple, possibly the result of ongoing wrapping by orbital evolution of particles in the initially tilted ring. From the wavelength of the wrap, which shortens with time, the event was dated to the early 1980s (*56*). The ripple was later found to extend through the C ring (*55*), indicating that the tilt was imposed by an impacting stream of rubble, perhaps from a disrupted comet 1 to 10 km in size with an extended node crossing the D and C rings. The event may have had two parts, separated by months (*57*). There is also evidence in Voyager data for two other disturbances that occurred in 1979 (*58*). All this sporadic disruption could plausibly have altered the properties of the D ring in such a way that today's flux (and/or today's D ring) are not necessarily typical of the last 100 million years. We expect these events to have happened at the same average rate going backward, producing variability in the D ring.

Our results for the delivery of ring materials have implications for the composition of Saturn's deep atmosphere (stratosphere and troposphere). Previous modeling (*7*) has suggested that the delivery of oxygen, in the form of water, can explain the presence of CO seen in the stratosphere. In addition to water, we observe carbon monoxide and carbon dioxide influx that can contribute to the oxygen inventory (Fig. 6).

Because of the influx of CH_4 and other sources of carbon, Saturn may have acquired an apparent methane enrichment (i.e., higher C/H ratio) relative to the protosolar value. Observations using the CIRS instrument onboard Cassini indicate that Saturn's methane enrichment over the protosolar value is 2.25 ± 0.55 times the enrichment seen in Jupiter (*59*). Our INMS observations indicate an influx of methane between 3×10^{28} and 2×10^{29} molecules per second entering the equatorial atmosphere, and 2.5 times as much mass in the form of other organics. If we assume that inflowing methane spreads over the globe, this is equivalent to an influx of 7×10^{11} to $4.8 \times 10^{12}\ m^{-2}\ s^{-1}$ throughout the atmosphere. By calculating the column density of methane in the thermosphere, stratosphere, and troposphere above an altitude of 50 km, where the contribution function of CIRS peaked (*59*), we can estimate how long the observed methane influx from the rings would need to be sustained to raise the enrichment to 2.25 times that of Jupiter. The estimated time is ~7 million to 110 million years—within approximately an order of magnitude of the estimated lifetime of the rings themselves (see above). This slow buildup occurs in the stratosphere and troposphere, because the predominant methane flux at this altitude is from the deep interior produced by recycled heavier hydrocarbons that photochemically formed in the stratosphere and later diffused down into the interior. Thus, the methane flux from above provides a very slow shift in the steady-state concentration that builds up over time in the stratosphere and troposphere. The organic carbon nanograin material, with a mass influx 2.5 times that of methane, could be chemically recycled deep in the atmosphere to increase the methane content in the deeper interior and drive a larger interior outflux of methane. However, our derived infalling material composition (Fig. 6) includes influx of NH_3, and it is unclear whether prolonged, continuous delivery of ring-derived NH_3 would be consistent with existing upper limits on the $^{15}N/^{14}N$ ratio in Saturn (*60*).

Conclusions

The Cassini INMS measured in situ the atmospheric and ionospheric composition of Saturn's equatorial atmosphere during a series of flybys between the atmosphere and the D ring in the Grand Finale phase of the mission. Water, methane, ammonia, carbon monoxide and/or molecular nitrogen, and carbon dioxide enter Saturn's atmosphere from the D ring along the ring plane. This influx is expected to affect the equatorial ionospheric chemistry by converting the H^+ and H_3^+ ions into heavier molecular ions, producing a depletion of ionospheric density previously observed in radio occultation observations (*10*). However, this may not explain the full extent of small-scale electron depletions observed by other Cassini instruments (*33*). INMS data include evidence for an influx of organic-rich nanoparticles that further modifies the composition and structure of the equatorial ionosphere and may circulate throughout the low- and mid-latitude thermosphere. Over long time scales, this infalling material may affect the carbon and oxygen content of the observed atmosphere.

Methods

The data on the D68 ringlet brightness distribution (Fig. 5) are from a sequence of images obtained by the Imaging Science Subsystem (ISS) onboard the Cassini spacecraft on day 229 of 2017, during rev 289. All images were calibrated using the standard CISSCAL routines, which remove dark currents, apply flat-field corrections, and convert the observed brightness data to I/F, a standardized measure of reflectance that is unity for a surface illuminated and viewed at normal incidence (*62*, *63*). These calibrated images were geometrically transformed with the appropriate SPICE kernels (*64*), and the pointing was refined on the basis of the observed locations of stars in the field of view (*27*). For each image, the brightness data were then reprojected onto regular grids of radii and inertial longitude (i.e., longitude measured relative to the ascending node of the rings in the J2000 coordinate system). Each column of the reprojected maps then provides a radial profile of D68 at a single inertial longitude. Radial profiles were co-added to generate longitudinal brightness profiles. Because the ring material orbits the planet, these profiles are constructed in a corotating longitude system with an assumed mean motion of 1751.7° per day and a reference epoch time of 300000000 TDB (Barycentric Dynamical Time), which is 2009-185T17:18:54 UTC (Coordinated Universal Time).

The Cassini images did not have sufficient spatial resolution to discern D68's internal structure, so the ringlet's brightness is quantified in terms of its equivalent width (EW), which is the radially integrated I/F of the ringlet over the radius range 67,550 to 67,700 km above a background level given by a linear fit to the signal levels on either side of the ringlet (67,000 to 67,500 km and 67,750 to 68,250 km, respectively). The estimates of the ringlet's equivalent width are converted to normal equivalent width (NEW) by multiplying the EW values by the cosine of the ring's emission angle. For features with low optical depth such as D68, NEW is independent of ring opening angle.

REFERENCES AND NOTES

1. J. H. Waite Jr., S. K. Atreya, A. F. Nagy, The ionosphere of Saturn: Predictions for Pioneer 11. *Geophys. Res. Lett.* **6**, 723–726 (1979). doi: 10.1029/GL006i009p00723
2. A. J. Kliore *et al.*, Structure of the ionosphere and atmosphere of Saturn From Pioneer 11 Saturn radio occultation. *J. Geophys. Res.* **85**, 5857–5870 (1980). doi: 10.1029/JA085iA11p05857
3. G. L. Tyler *et al.*, Radio science with Voyager 2 at Saturn: Atmosphere and ionosphere and the masses of Mimas, Tethys, and Iapetus. *Science* **215**, 553–558 (1982). doi: 10.1126/science.215.4532.553; pmid: 17771277
4. M. L. Kaiser, M. D. Desch, J. E. P. Connerney, Saturn's ionosphere: Inferred electron densities. *J. Geophys. Res.* **89**, 2371–2376 (1984). doi: 10.1029/JA089iA04p02371
5. J. E. P. Connerney, Magnetic connection for Saturn's rings and atmosphere. *Geophys. Res. Lett.* **13**, 773–776 (1986). doi: 10.1029/GL013i008p00773
6. J. E. P. Connerney, J. H. Waite, New model of Saturn's ionosphere with an influx of water from the rings. *Nature* **312**, 136–138 (1984). doi: 10.1038/312136a0
7. J. I. Moses, S. F. Bass, The effects of external material on the chemistry and structure of Saturn's ionosphere. *J. Geophys. Res.* **105**, 7013–7052 (2000). doi: 10.1029/1999JE001172
8. L. Moore, I. Mueller-Wodarg, M. Galand, A. Kliore, M. Mendillo, Latitudinal variations in Saturn's ionosphere: Cassini measurements and model comparisons. *J. Geophys. Res.* **115**, A11317 (2010). doi: 10.1029/2010JA015692
9. J. O'Donoghue *et al.*, The domination of Saturn's low-latitude ionosphere by ring 'rain'. *Nature* **496**, 193–195 (2013). doi: 10.1038/nature12049; pmid: 23579676
10. A. J. Kliore *et al.*, The ionosphere of Saturn as observed by the Cassini Radio Science System. *Geophys. Res. Lett.* **41**, 5778–5782 (2014). doi: 10.1002/2014GL060512
11. J. H. Waite Jr. *et al.*, The Cassini Ion and Neutral Mass Spectrometer (INMS) Investigation. *Space Sci. Rev.* **114**, 113–231 (2004). doi: 10.1007/s11214-004-1408-2
12. I. C. F. Müller-Wodarg, L. Moore, M. Galand, S. Miller, M. Mendillo, Magnetosphere–atmosphere coupling at Saturn: 1 – Response of thermosphere and ionosphere to steady state polar forcing. *Icarus* **221**, 481–494 (2012). doi: 10.1016/j.icarus.2012.08.034
13. T. T. Koskinen *et al.*, Saturn's variable thermosphere from Cassini/UVIS occultations. *Icarus* **260**, 174–189 (2015). doi: 10.1016/j.icarus.2015.07.008
14. B. D. Teolis *et al.*, A Revised Sensitivity Model for Cassini INMS: Results at Titan. *Space Sci. Rev.* **190**, 47–84 (2015). doi: 10.1007/s11214-014-0133-8
15. R. V. Yelle *et al.*, Thermal Structure and Composition of Saturn's Upper Atmosphere from Cassini/INMS Measurements. *Geophys. Res. Lett.* 10.1029/2018GL078454 (2018).
16. D. Mitchell *et al.*, Dust grains fall from Saturn's D-ring into its equatorial upper atmosphere. *Science* **362**, eaat2236 (2018).
17. M. M. Hedman, J. A. Burt, J. A. Burns, M. R. Showalter, Non-circular features in Saturn's D ring: D68. *Icarus* **233**, 147–162 (2014). doi: 10.1016/j.icarus.2014.01.022
18. J. de Maaijer-Gielbert, Á. Somogyi, V. H. Wysocki, P. G. Kistemaker, T. L. Weeding, Surface-induced dissociation of diphenyl ether. *Int. J. Mass Spectrom.* **174**, 81–94 (1998). doi: 10.1016/S0168-1176(97)00292-9
19. A. W. Kleyn, Dissociation in molecule-surface collisions. *J. Phys. Condens. Matter* **4**, 8375–8394 (1992). doi: 10.1088/0953-8984/4/44/003
20. A. Forni, G. Wiesenekker, E. J. Baerends, G. F. Tantardini, A dynamical study of the chemisorption of molecular hydrogen on the Cu(111) surface. *J. Phys. Condens. Matter* **7**, 7195–7207 (1995). doi: 10.1088/0953-8984/7/36/009
21. B. Teolis, M. E. Perry, B. A. Magee, J. Westlake, J. H. Waite, Detection and measurement of ice grains and gas distribution in the Enceladus plume by Cassini's Ion Neutral Mass Spectrometer. *J. Geophys. Res.* **115**, A09222 (2010). doi: 10.1029/2009JA015192
22. B. A. Magee *et al.*, INMS-derived composition of Titan's upper atmosphere: Analysis methods and model comparison. *Planet. Space Sci.* **57**, 1895–1916 (2009). doi: 10.1016/j.pss.2009.06.016
23. S. E. Stein, "Mass Spectra," in *NIST Chemistry WebBook, NIST Standard Reference Database Number 69*, P. J. Linstrom, W.G. Mallard, Eds. (National Institute of Standards and Technology); https://webbook.nist.gov/chemistry/.
24. M. E. Perry *et al.*, Material flux from the rings of Saturn into its atmosphere. *Geophys. Res. Lett.* 10.1029/2018GL078575 (2018).
25. S. A. Sandford *et al.*, Organics captured from comet 81P/Wild 2 by the Stardust spacecraft. *Science* **314**, 1720–1724 (2006). doi: 10.1126/science.1135841; pmid: 17170291
26. C. K. Materese, D. P. Cruikshank, S. A. Sandford, H. Imanaka, M. Nuevo, Ice chemistry on outer solar system bodies: Electron radiolysis of N_2-, CH_4-, and CO-containing ices. *Astrophys. J.* **812**, 150 (2015). doi: 10.1088/0004-637X/812/2/150
27. R. L. Hudson, M. E. Palumo, G. Strazzulla, M. H. Moore, J. F. Cooper, S. J. Sturner, in *The Solar System Beyond Neptune*, M. A. Barucci, H. Boehnhardt, D. P. Cruikshank, A. Morbidelli, Eds. (Univ. of Arizona Press, 2008), pp. 507–523.
28. P. M. Banks, G. Kockarts, *Aeronomy* (Academic Press, 1973).
29. J. M. Bell *et al.*, Developing a self-consistent description of Titan's upper atmosphere without hydrodynamic escape. *J. Geophys. Res.* **119**, 4957–4972 (2014). doi: 10.1002/2014JA019781
30. B. G. Higgins, H. Binous, "Binary Diffusion Coefficients for Gases" (Wolfram Demonstrations Project, 2013); http://demonstrations.wolfram.com/BinaryDiffusionCoefficientsForGases.
31. L. Z. Hadid *et al.*, Saturn's ionosphere: Electron density altitude profiles and D ring interaction from the Cassini Grand Finale. *Geophys. Res. Lett.* 10.1029/2018GL078004 (2018).
32. A. M. Persoon *et al.*, Electron density distributions in Saturn's ionosphere. *Geophys. Res. Lett.* 10.1029/2018GL078020 (2018).
33. J.-E. Wahlund *et al.*, In situ measurements of Saturn's ionosphere show that it is dynamic and interacts with the rings. *Science* **359**, 66–68 (2018). doi: 10.1126/science.aao4134; pmid: 29229651
34. T. E. Cravens, L. Moore, J. H. Waite Jr., R. Perryman, M. Perry, J.-E. Wahlund, A. Persoon, W. S. Kurth, The Ion Composition of Saturn's Equatorial Ionosphere as Observed by Cassini. *Geophys. Res. Lett.* (2018). doi: 10.1029/2018GL077868
35. T. Koskinen, S. Guerlet, Atmospheric structure and helium abundance on Saturn from Cassini/UVIS and CIRS observations. *Icarus* **307**, 161–171 (2018). doi: 10.1016/j.icarus.2018.02.020
36. J. M. Bell *et al.*, Simulating the one-dimensional structure of Titan's upper atmosphere: 1. Formulation of the Titan Global Ionosphere-Thermosphere Model and benchmark simulations. *J. Geophys. Res.* **115**, E12002 (2010). doi: 10.1029/2010JE003636
37. A. J. Ridley, Y. Deng, G. Tóth, The global ionosphere–thermosphere model. *J. Atmos. Sol. Terr. Phys.* **68**, 839–864 (2006). doi: 10.1016/j.jastp.2006.01.008
38. B. J. Conrath, D. Gautier, R. A. Hanel, J. S. Hornstein, The helium abundance of Saturn from Voyager measurements. *Astrophys. J.* **282**, 807–815 (1984). doi: 10.1086/162267
39. L. Ben-Jaffel, I. Abbes, Helium abundance in giant planets and the local interstellar medium. *J. Phys. Conf. Ser.* **577**, 012003 (2015). doi: 10.1088/1742-6596/577/1/012003
40. D. J. Stevenson, E. E. Salpeter, The dynamics and helium distribution in hydrogen-helium fluid planets. *Astrophys. J. Suppl. Ser.* **35**, 239–261 (1977). doi: 10.1086/190479

41. M. Asplund, N. Grevesse, A. J. Sauval, P. Scott, The Chemical Composition of the Sun. *Annu. Rev. Astron. Astrophys.* **47**, 481–522 (2009). doi: 10.1146/annurev.astro.46.060407.145222
42. U. von Zahn, D. M. Hunten, G. Lehmacher, Helium in Jupiter's atmosphere: Results from the Galileo probe Helium Interferometer Experiment. *J. Geophys. Res.* **103**, 22815–22829 (1998). doi: 10.1029/98JE00695
43. J. J. Fortney, W. B. Hubbard, Phase separation in giant planets: Inhomogeneous evolution of Saturn. *Icarus* **164**, 228–243 (2003). doi: 10.1016/S0019-1035(03)00130-1
44. B. J. Conrath, D. Gautier, Saturn Helium Abundance: A Reanalysis of Voyager Measurements. *Icarus* **144**, 124–134 (2000). doi: 10.1006/icar.1999.6265
45. L. Moore *et al*., Models of Saturn's equatorial ionosphere based on in situ data from Cassini's Grand Finale. *Geophys. Res. Lett.* 10.1029/2018GL078162 (2018).
46. D. R. Bates, Dissociative recombination of polyatomic ions. *J. Phys. B* **24**, 3267–3284 (1991). doi: 10.1088/0953-4075/24/14/019
47. R. W. Schunk, A. F. Nagy, *Ionospheres: Physics, Plasma Physics, and Chemistry* (Cambridge Univ. Press, ed. 2, 2009).
48. D. Bockelée-Morvan, An overview of comet composition. *Proc. IAU* **7**, 261–274 (2011). doi: 10.1017/S1743921311025038
49. M. M. Hedman, P. D. Nicholson, More Kronoseismology with Saturn's rings. *Mon. Not. R. Astron. Soc.* **444**, 1369–1388 (2014). doi: 10.1093/mnras/stu1503
50. M. M. Hedman, F. Postberg, D. P. Hamilton, S. Renner, H.-W. Hsu, in *Planetary Ring Systems*, M. Tiscareno, C. Murray, Eds. (Cambridge Univ. Press, 2018), pp. 308–337.
51. Scaling the A ring viscosity ν from (*61*) by the ratio of C ring to A ring optical depths, and assuming a spreading time $t = D^{2/\nu}$, where ν is viscosity and D is the width of the C ring, the spreading time is comparable to the age of the Solar System, much longer than the currently believed age of the rings.
52. M. M. Hedman, P. D. Nicholson, The B-ring's surface mass density from hidden density waves: Less than meets the eye? *Icarus* **279**, 109–124 (2016). doi: 10.1016/j.icarus.2016.01.007
53. J. N. Cuzzi, P. R. Estrada, Compositional Evolution of Saturn's Rings Due to Meteoroid Bombardment. *Icarus* **132**, 1–35 (1998). doi: 10.1006/icar.1997.5863
54. S. Charnoz, L. Dones, L. W. Esposito, P. R. Estrada, M. M. Hedman, in *Saturn from Cassini-Huygens*, M. K. Dougherty, L. W. Esposito, S. M. Krimigis, Eds. (Springer, 2009), pp. 537–575.
55. M. M. Hedman, J. A. Burns, M. W. Evans, M. S. Tiscareno, C. C. Porco, Saturn's curiously corrugated C ring. *Science* **332**, 708–711 (2011). doi: 10.1126/science.1202238; pmid: 21454753
56. M. M. Hedman *et al*., Saturn's dynamic D ring. *Icarus* **188**, 89–107 (2007). doi: 10.1016/j.icarus.2006.11.017
57. M. M. Hedman, J. A. Burns, M. R. Showalter, Corrugations and eccentric spirals in Saturn's D ring: New insights into what happened at Saturn in 1983. *Icarus* **248**, 137–161 (2015). doi: 10.1016/j.icarus.2014.10.021
58. M. M. Hedman, M. R. Showalter, A new pattern in Saturn's D ring created in late 2011. *Icarus* **279**, 155–165 (2016). doi: 10.1016/j.icarus.2015.09.017
59. L. N. Fletcher, G. S. Orton, N. A. Teanby, P. G. J. Irwin, G. L. Bjoraker, Methane and its isotopologues on Saturn from Cassini/CIRS observations. *Icarus* **199**, 351–367 (2009). doi: 10.1016/j.icarus.2008.09.019
60. L. N. Fletcher *et al*., The origin of nitrogen on Jupiter and Saturn from the ^{15}N/^{14}N ratio. *Icarus* **238**, 170–190 (2014). doi: 10.1016/j.icarus.2014.05.007
61. J. E. Colwell, P. D. Nicholson, M. S. Tiscareno, C. D. Murray, R. G. French, E. A. Marouf, in *Saturn from Cassini-Huygens*, M. K. Dougherty, L. W. Esposito, S. M. Krimigis, Eds. (Springer, 2009), pp. 375–412.
62. C. C. Porco *et al*., Cassini Imaging Science: Instrument Characteristics and Anticipated Scientific Investigations at Saturn. *Space Sci. Rev.* **115**, 363–497 (2004). doi: 10.1007/s11214-004-1456-7
63. R. West *et al*., In-flight calibration of the Cassini imaging science sub-system cameras. *Planet. Space Sci.* **58**, 1475–1488 (2010). doi: 10.1016/j.pss.2010.07.006
64. C. H. Acton Jr., Ancillary data services of NASA's Navigation and Ancillary Information Facility. *Planet. Space Sci.* **44**, 65–70 (1996). doi: 10.1016/0032-0633(95)00107-7

ACKNOWLEDGMENTS

We gratefully acknowledge the support of the Cassini project in the flawless execution of the Cassini Grand Finale phase; the late Hasso Niemann and his NASA GSFC team that built a superb mass spectrometer that produced beautiful data for many years; and the INMS operations team who operated the INMS equally flawlessly through most of the mission. **Funding:** Work performed by the Cassini INMS team was supported by NASA JPL subcontract (NASA contract NAS703001TONMO711123, JPL subcontract 1405853) and INMS science support grant NNX13AG63G (M.E.P.). J.-E.W., L.Z.H., and M.M. were supported by the Swedish National Space Board (SNSB) for work and data from the RPWS/LP instrument on board Cassini; research at the University of Iowa was supported by NASA through contract 1415150 with the Jet Propulsion Laboratory. J.C. was also supported by the Cassini project through his Interdisciplinary Scientist grant, NASA WBS 431924.02.01.02. D.G.M. was supported for his contribution by the NASA Office of Space Science under Task Order 003 of contract NAS5-97271 between NASA Goddard Space Flight Center and Johns Hopkins University. W.T. was supported by Taiwan Ministry of Science and Technology grant 106-2112-M-003-015. **Author contributions:** J.H.W., R.S.P., and M.E.P. planned the observations and discussed their value in the Cassini Grand Finale phase of the mission; R.S.P. led the instrument operations uplink and downlink process; R.S.P., M.E.P., K.E.M., T.E.C., R.Y., and J.H.W. contributed to the analysis of the dataset; J.H.W., R.S.P., K.E.M., T.E.C., J.B., C.R.G., and M.E.P. wrote the initial text; J.H.W., K.E.M., T.B., J.W., S.C., B.T., and J.G. contributed to modeling and/or experiments concerning the interaction of the gas with the INMS antechamber at high impact velocity (fragmentation, chemisorption, and physisorption processes); M.H., J.C., O.J.T., R.J., S.L., W.-H.I., and W.T. provided information about the rings and their associated atmosphere; D.G.M. and M.E.P. provided insight into the equatorial ice grains from the Cassini MIMI investigation; W.S.K., J.-E.W., L.Z.H., M.M., and A.P. provided complementary information about the ionosphere as measured by the Cassini RPWS investigation; T.E.C., A.N., and L.M. provided ionospheric modeling; and J.B. and R.Y. provided atmospheric modeling. All authors contributed to revising and editing of the text. **Competing interests:** The authors declare no competing interests. **Data and materials availability:** INMS data from the Grand Finale phase of the Cassini mission are available on NASA's Planetary Data System at https://pds-ppi.igpp.ucla.edu/search/view/?f=yes&id=pds://PPI/CO-S-INMS-3-L1A-U-V1.0/DATA/SATURN/2017. We used data from 2017-111 to 2017-258.

6 February 2018; accepted 10 September 2018
10.1126/science.aat2382

Science

Chemical interactions between Saturn's atmosphere and its rings

J. H. Waite Jr., R. S. Perryman, M. E. Perry, K. E. Miller, J. Bell, T. E. Cravens, C. R. Glein, J. Grimes, M. Hedman, J. Cuzzi, T. Brockwell, B. Teolis, L. Moore, D. G. Mitchell, A. Persoon, W. S. Kurth, J.-E. Wahlund, M. Morooka, L. Z. Hadid, S. Chocron, J. Walker, A. Nagy, R. Yelle, S. Ledvina, R. Johnson, W. Tseng, O. J. Tucker and W.-H. Ip

Science **362** (6410), eaat2382.
DOI: 10.1126/science.aat2382

Cassini's final phase of exploration

The Cassini spacecraft spent 13 years orbiting Saturn; as it ran low on fuel, the trajectory was changed to sample regions it had not yet visited. A series of orbits close to the rings was followed by a Grand Finale orbit, which took the spacecraft through the gap between Saturn and its rings before the spacecraft was destroyed when it entered the planet's upper atmosphere. Six papers in this issue report results from these final phases of the Cassini mission. Dougherty *et al.* measured the magnetic field close to Saturn, which implies a complex multilayer dynamo process inside the planet. Roussos *et al.* detected an additional radiation belt trapped within the rings, sustained by the radioactive decay of free neutrons. Lamy *et al.* present plasma measurements taken as Cassini flew through regions emitting kilometric radiation, connected to the planet's aurorae. Hsu *et al.* determined the composition of large, solid dust particles falling from the rings into the planet, whereas Mitchell *et al.* investigated the smaller dust nanograins and show how they interact with the planet's upper atmosphere. Finally, Waite *et al.* identified molecules in the infalling material and directly measured the composition of Saturn's atmosphere.

Science, this issue p. eaat5434, p. eaat1962, p. eaat2027, p. eaat3185, p. eaat2236, p. eaat2382

Science (print ISSN 0036-8075; online ISSN 1095-9203) is published by the American Association for the Advancement of Science, 1200 New York Avenue NW, Washington, DC 20005.